Myxobacteria gliding motility requires cytoskeleton rotation powered by proton motive force

Beiyan Nan[a], Jing Chen[b], John C. Neu[c], Richard M. Berry[d], George Oster[a,1], and David R. Zusman[a,1]

Departments of [a]Molecular and Cell Biology and [c]Mathematics, and [b]Biophysics Graduate Group, University of California, Berkeley, CA 94720; and [d]Department of Physics, University of Oxford, Oxford OX1 3PU, United Kingdom

Contributed by George Oster, December 23, 2010 (sent for review November 4, 2010)

Myxococcus xanthus **is a Gram-negative bacterium that glides over surfaces without the aid of flagella. Two motility systems are used for locomotion: social-motility, powered by the retraction of type IV pili, and adventurous (A)-motility, powered by unknown mechanism(s). We have shown that AgmU, an A-motility protein, is part of a multiprotein complex that spans the inner membrane and periplasm of *M. xanthus*. In this paper, we present evidence that periplasmic AgmU decorates a looped continuous helix that rotates clockwise as cells glide forward, reversing its rotation when cells reverse polarity. Inhibitor studies showed that the AgmU helix rotation is driven by proton motive force (PMF) and depends on actin-like MreB cytoskeletal filaments. The AgmU motility complex was found to interact with MotAB homologs. Our data are consistent with a mechanochemical model in which PMF-driven motors, similar to bacterial flagella stator complexes, run along an endless looped helical track, driving rotation of the track; deformation of the cell surface by the AgmU-associated proteins creates pressure waves in the slime, pushing cells forward.**

Myxobacteria live in soil and have a complex life cycle that includes vegetative swarming, predation, and fruiting body formation. These activities are facilitated by two gliding motility systems: social (S)-motility and adventurous (A)-motility (1). S-motility is primarily involved in the movement of cells in groups and is powered by the retraction of type IV pili, similar to twitching motility in *Pseudomonas aeruginosa* (2–4). A-motility is required for the movement of isolated cells. Despite the identification of ≈40 A-motility related genes (5–7) and several intriguing hypotheses (8, 9), the mechanism of A-motility remains elusive.

We have been studying the motility mechanism in *Myxococcus xanthus* and the *frizzy* (Frz) chemosensory system that controls cell reversals. FrzCD, the chemoreceptor for the Frz pathway, contains an unusual N-terminal domain that interacts with two A-motility proteins: AglZ, a cytoplasmic protein, and AgmU, a protein that localizes to both the cytoplasm and periplasm (10, 11). *aglZ* and *agmU* mutants are defective in A-motility but show normal S-motility (11, 12). Cytoplasmic AgmU-mCherry colocalizes with AglZ-YFP (yellow fluorescent protein) in moving cells as distributed arrays of fluorescent clusters. Surprisingly, these clusters appear stationary as cells move forward (9, 11). Recently, we found that AgmU is also associated with many other A-motility proteins including AglT, AgmK, AgmX, AglW, and CglB. These proteins likely form a large multiprotein complex that spans the membrane and periplasm of the cells (11). Here, we report that periplasmic AgmU decorates a closed looped helix that rotates as cells move forward. Rotation depended on proton motive force (PMF) and an intact MreB cytoskeleton. Based on our findings, we propose a model of gliding motility in which MotAB homologs and associated motility proteins push against an endless looped helical track, driving the rotation of the track and the translocation of the cell.

Results and Discussion

Periplasmic AgmU Decorates a Looped Helix. To visualize periplasmic AgmU, we used a fluorescently labeled *agmU::mCherry* strain that showed no defects in motility or fruiting body formation (11). Fig. 1*A* shows deconvolved fluorescence images from a fixed cell; 3D reconstructions of AgmU:mCherry fluorescence from ≈20 images show that AgmU-mCherry forms a twisted endless looped helix that spans the length of the cells (Fig. 1*B*). The distance between adjacent nodes is 0.45 ± 0.09 μm (average of 10 cells), nearly identical to that of *M. xanthus* MreB helices, 0.47 ± 0.1 μm (13). Considering AgmU as a closed helical loop, the period of this helix is ≈0.7–1.1 μm.

AgmU-mCherry Helices Rotate as Cells Move on Hard Agar Surfaces. We also followed live *pilA*$^-$ *agmU-mCherry* (A^+S^- motile) cells by fluorescence video microscopy. We observed that the AgmU-mCherry helix rotates as cells move on a 1.5% agar surface and that the direction of rotation reverses when cells reverse their direction (Movies S1 and S2). Viewed from the lagging cell pole, the AgmU-mCherry helix always rotates clockwise. Additionally, the concentration of AgmU-mCherry is higher at the leading cell pole. When cells reverse, AgmU-mCherry relocalizes to the new leading cell pole within a few seconds (Fig. 1*C* and Movies S1 and S2). To exclude the possibility that the apparent rotational motion is an illusion caused by the uneven agar surface or the gliding motion itself, we suspended the *pilA*$^-$ *agmU::mCherry* cells in liquid culture or 1% methylcellulose solution and imaged the fluorescence at 2-s intervals. Without a surface for gliding, cells are stationary. Nevertheless, the AgmU-mCherry helical fluorescence continued to rotate as on agar surfaces (Movie S3). This rotation is illustrated in Fig. 1*D*, where the image of one frame (red; Fig. 1*D, Left*) is merged with a frame recorded 2 s later (green; Fig. 1*D, Middle*). During the 2-s time interval between images, the AgmU helix and the pitch remained unchanged, but the helix from each frame showed a clear shift compared with the previous frame (Fig. 1*D, Right*), consistent with rotation.

Because of the complexity of the images, we were unable to determine the rotational speed of the AgmU helices when viewed laterally. However, some cells in liquid culture or methylcellulose were perpendicular to the focal plane, yielding an end-on view. AgmU in these cells appeared as discontinuous circles because of changes in the depth of field, consistent with a looped helical structure. With this fluorescence discontinuity as a reference, we were able to determine the rotational speed of the AgmU helix by calculating the angular velocity of the discontinuity. Fig. 1*E* and Movie S4 show a rotational speed of ≈8.4 rpm; the average rotational speed from five individual cells was 7.5 ± 1.2 rpm. Because the AgmU helix shows a 0.7- to 1.1-μm period, the calculated linear velocity of cells would be ≈4.4–9.6 μm/min, consistent with the maximum velocity of A-motility, ≈2–4 μm/min

Author contributions: B.N., J.C., R.M.B., G.O., and D.R.Z. designed research; B.N., J.C., and R.M.B. performed research; B.N., J.C., J.C.N., R.M.B., and G.O. analyzed data; and B.N., J.C., G.O., and D.R.Z. wrote the paper.

The authors declare no conflict of interest.

[1]To whom correspondence may be addressed. E-mail: goster@berkeley.edu or zusman@berkeley.edu.

This article contains supporting information online at www.pnas.org/lookup/suppl/doi:10.1073/pnas.1018556108/-/DCSupplemental.

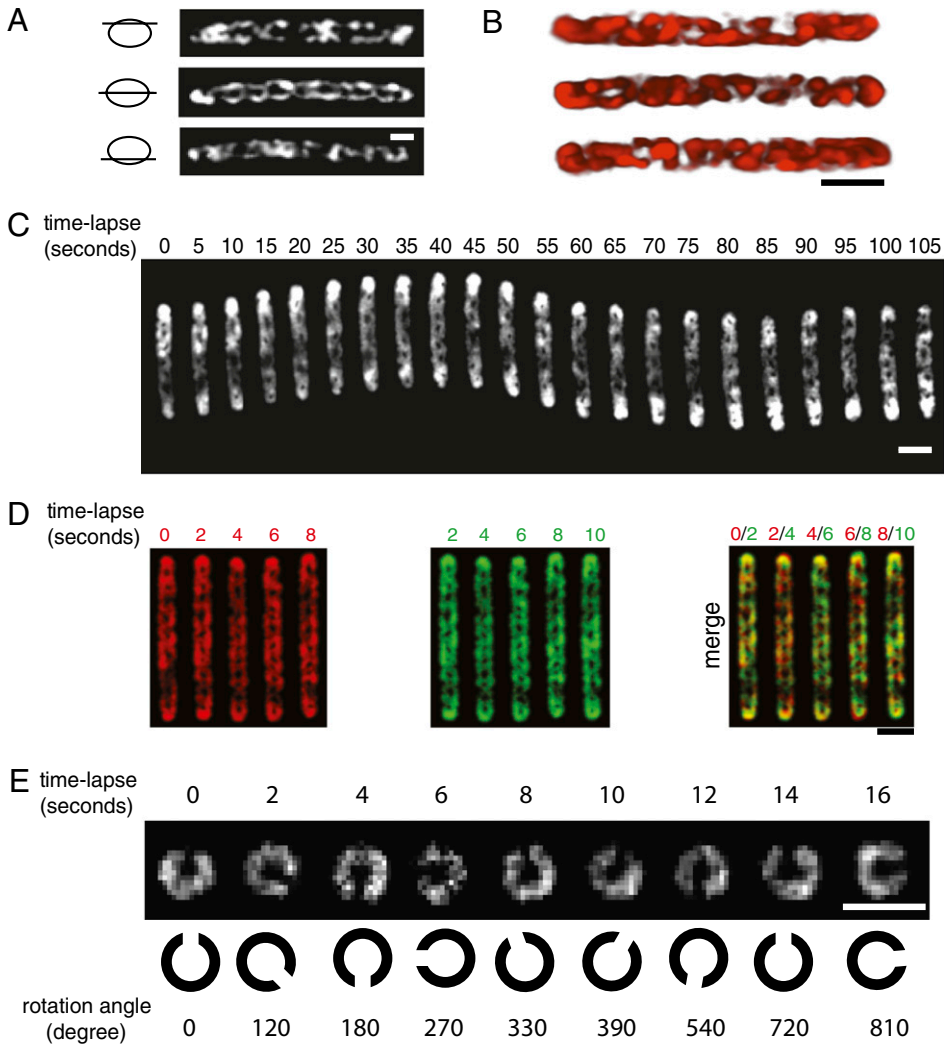

Fig. 1. Images of AgmU. (*A*) Deconvolved images of one fixed *agmU::mCherry* cell. (*B*) Three-dimensional reconstructions of the AgmU helix from three individual cells. (*C*) Time-lapse images of AgmU-mCherry in a moving cell. The bright clusters indicate the leading cell pole, which shifts to the opposite pole when cells reverse. (*D*) Time-lapse images of *agmU-mCherry pilA* cells in 1% methylcellulose. To visualize movement, one frame (red; *Left*) is merged (*Right* with a frame recorded 2 s later (green; *Center*). (*E*) Polar time-lapse views of an *agmU::mCherry pilA* cell in 1% methylcellulose. (Scale bars: 1 μm.)

(14). The helix may slip relative to the surface, or, alternatively, its rotation may be slower when the cell is associated with a surface.

Rotation of the AgmU Helix Is Driven by PMF. To determine the force driving the rotation of the AgmU helices, we followed the movement of cells and the rotation of AgmU helices in *pilA*$^-$ *agmU::mCherry* cells treated with carbonyl cyanide-m-chlorophenylhydrazone (CCCP, 20 μM, to disrupt the PMF) or sodium azide (NaN_3, 80 mM, to disrupt ATP synthesis). In the presence of azide, both gliding motility and helix rotation continued for at least 30 min (Movie S5). After 60 min, most cells stopped moving, although helix rotation continued (Movie S6). By contrast, CCCP treatment stopped motility and helix rotation within 5 min (Fig. 2*A* and Movie S7). CCCP functions as a proton carrier that discharges both the electric potential and the pH gradient of PMF. We therefore treated the *pilA*$^-$ *agmU::mCherry* cells with nigericin or valinomycin. Nigericin reduces the pH gradient across the membrane, whereas valinomycin acts as a K^+-ionophore, discharging the membrane potential. Fig. 2*B* and Movie S8 show that nigericin (100 μM) stopped both A-motility and the rotation of AgmU helices within 10 min, whereas valinomycin (50 μM, in the presence of 150 mM KCl) had no effect on A-motility or AgmU helix rotation, even after 1 h (Fig. 2*C* and Movie S9). These preliminary data show that the pH gradient across the membrane might be the major component of the PMF, which drives both A-motility and the rotation of the AgmU helices.

We used fluorescence recovery after photobleaching (FRAP) to determine whether individual AgmU molecules are fixed to the helix or move relative to it. *M. xanthus agmU::mCherry pilA* cells were photobleached by exposure to bright laser illumination, with a section near the middle of the cell (≈1 μm) protected from photobleaching. Fluorescence recovered along the length of the cell within ≈10 s in untreated cells (Fig. 2*D* and Movies S10 and S11), but did not recover even after 5 min in cells treated with 20 μM CCCP (Fig. 2*E* and Movies S12 and S13). Thus, AgmU molecules move up and down the cell along a helical track, and this movement depends on the PMF.

Rotation of the AgmU Helix Requires an Intact MreB Cytoskeleton. AgmU helices are similar in both pitch and conformation with the actin-like cytoskeleton protein MreB. To see whether AgmU rotation depends on the MreB cytoskeleton, we treated *pilA*$^-$ *agmU::mCherry* cells with 100 μg/mL A22, an inhibitor of MreB polymerization and motility in *M. xanthus* (13). At this concen-

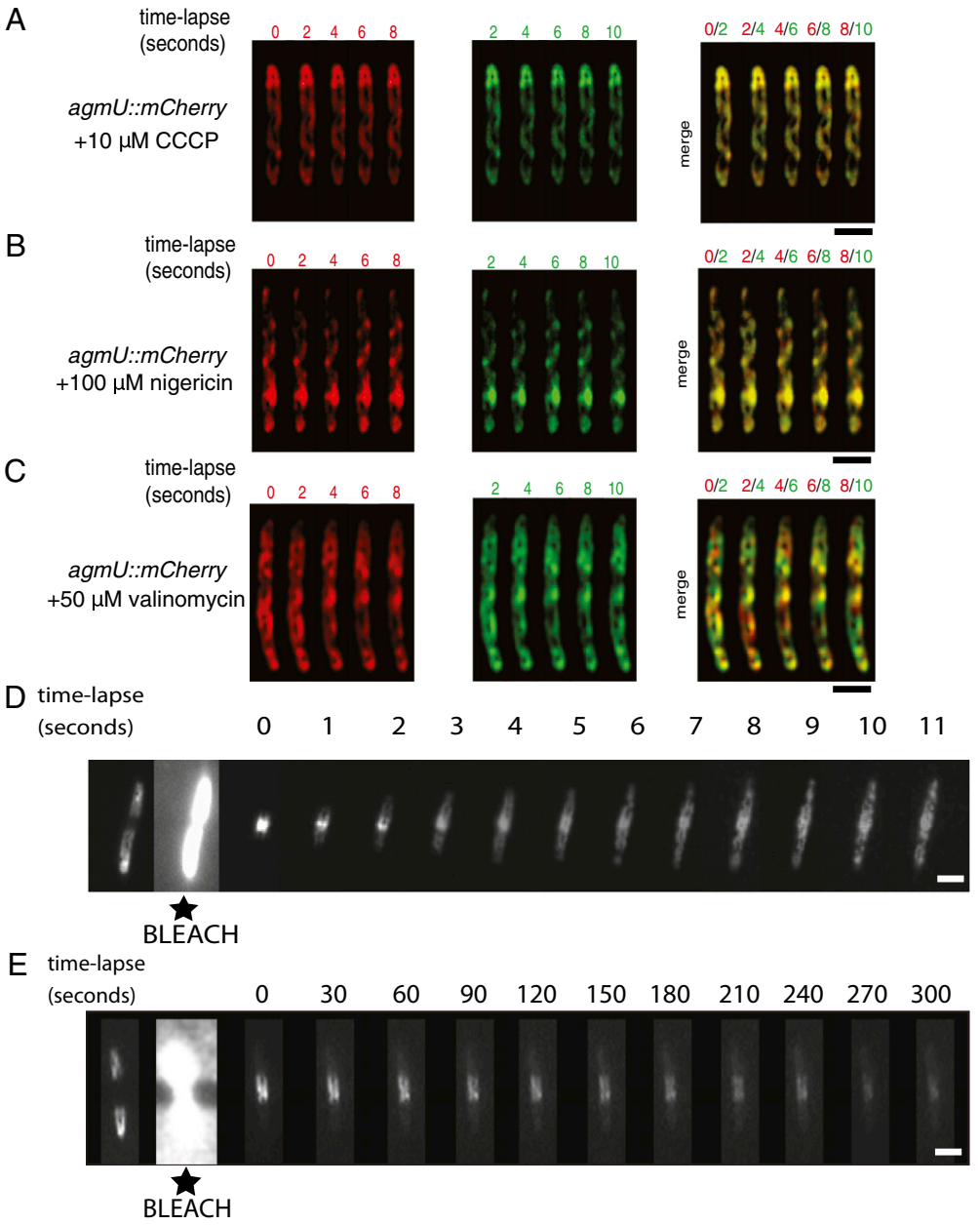

Fig. 2. The movements of the AgmU helix are powered by PMF. (*A–C*) Time-lapse images of *agmU-mCherry pilA* cells spotted on 1.5% agar containing CCCP (*A*), nigericin (*B*), or valinomycin (in the presence of 150 mM KCl) (*C*). Movements were visualized as in Fig. 1*D*. (*D* and *E*) FRAP. *agmU::mCherry pilA* cells were cultured in the absence (*D*) or presence (*E*) of CCCP. The cells were shielded with a ≈1-μm mask at their midsections and then bleached with a laser for 1 s. The recovery of fluorescence in the bleached cell poles was recorded at intervals. (Scale bars: 1 μm.)

tration, A22 abolished both A-motility and the rotation of AgmU within 10 min (Fig. 3*A* and Movie S14), whereas the helical localization pattern of AgmU remained largely unchanged. After longer incubation with A22 (>1 h), most of the cells lost their rod-like shape and the helical pattern of AgmU was disrupted (*SI Appendix*, Fig. S1*A*). A22 also prevented fluorescence recovery in FRAP experiments (Fig. 3*C* and Movie S15). By contrast, a strain carrying an A22-resistant mutation (*mreB*^{V323A}) (13) showed no defects in A-motility or AgmU helix rotation at a concentration of 200 μg/mL (Fig. 3*B* and Movie S16). NaN_3 treatment did not disrupt the MreB filaments (*SI Appendix*, Fig. S1 *B* and *C*). These data suggest that the MreB cytoskeleton is essential for the rotation of the AgmU helix. To investigate the possible involvement of peptidoglycan synthesis in the rotation of the AgmU helix, we treated the cells with cephalexin (100 μM, 8 h) or vancomycin (100 μM, 2 h). In both cases, no obvious change in the dynamics of AgmU was observed (Movies S17 and S18).

Cell Surface of *M. xanthus* Shows Helical Deformations That May Generate Translational Forces. We speculated that the associated A-motility proteins might distort the cell envelope and generate drag forces important for motility. We tested this prediction by total internal reflection fluorescence (TIRF) microscopy of *M. xanthus* cells expressing GFP in the cytoplasm (15). Cells were placed on glass microscope slides. TIRF images showed a modulation of intensity with a period of 0.85 ± 0.23 μm, similar to the periodicity of MreB helices and the other helical distributions of A-motility proteins reported above. Epifluorescence images

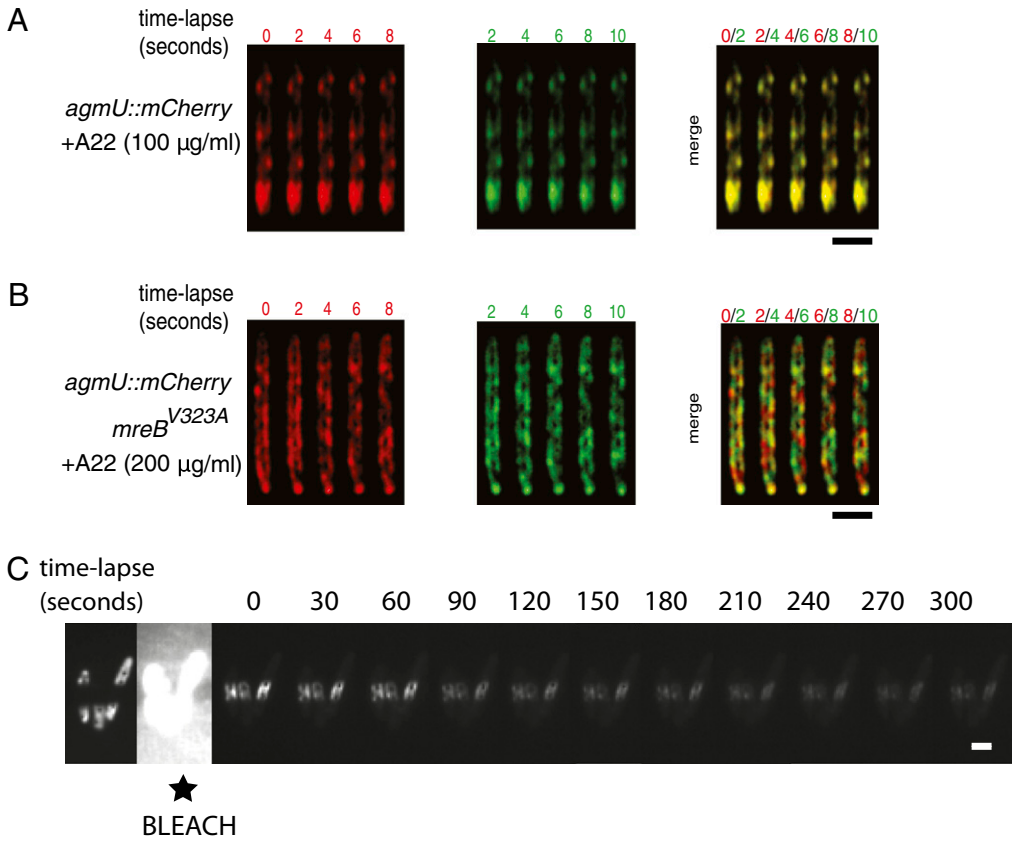

Fig. 3. AgmU helix movements require the MreB cytoskeleton. (*A* and *B*) Time-lapse images of *agmU::mCherry pilA* cells spotted on 1.5% agar containing A22. The rotation of the AgmU-mCherry helix stops after addition of A22 at 100 μg/mL (*A*). The rotation of AgmU-mCherry in cells carrying an A22-resistant mutation in the *mreB* gene (*mreB* ^{V323A}) is resistant to 200 μg/mL A22 (*B*). Movements were visualized as in Fig. 1*D*. (*C*) FRAP of *agmU::mCherry pilA* cells cultured in the presence (*C*) or absence (Fig. 2*D*) of A22 (100 μg/mL). FRAP experiments were performed as in Fig. 2 *D* and *E*. (Scale bars: 1 μm.)

showed GFP distributed evenly in the cytoplasm (Fig. 4). The TIRF images reflect periodic modulation of the distance between the cytoplasm and the glass. Thus, the presence of the helical track in the cell cytoplasm may be reflected in a helical contour on the surface of the cell, as observed by atomic force microscopy and scanning electron microscopy (16, 17).

MotAB Homologs Are Potential Candidates for A-Motility Motors. Flagella rotation is driven by motor proteins, MotAB, that use PMF to rotate the flagella filaments (18). We identified eight TolQ/TolR pairs in the *M. xanthus* genome that share homologies with MotA/MotB (19) (*SI Appendix*, Fig. S2). Two of the MotA/MotB pairs, AglX/AglV and AglR/AglS, were identified as essential for A-motility (5). We confirmed that *aglX* and *aglR* mutants show defects in A-motility (*SI Appendix*, Fig. S3). AglX and AglV proteins interact with each other and both interact with AgmU in affinity pull-down experiments (*SI Appendix*, Table S1). Additionally, AglX-mCherry and AglR-mCherry appear as rotating helices similar to AgmU (*SI Appendix*, Fig. S4 *A* and *B* and Movies S19 and S20), and their rotation is arrested by CCCP, nigericin, and A22 (*SI Appendix*, Fig. S4*C*). These results are consistent with a role for these MotA/MotB pairs in powering AgmU rotation and cell movement.

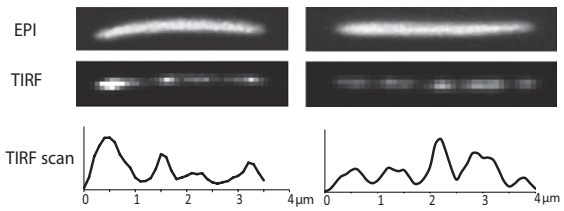

Fig. 4. Epifluorescence and TIRF microscopic images of cell surfaces. *M. xanthus* cells expressing GFP in the cytoplasm under the control of the *pilA* promoter were placed on glass microscope slides and imaged by epifluorescence and TIRF microscopy. Two typical cells are shown. The average distance between adjacent fluorescence peaks in the TIRF images is 0.85 ± 0.23 μm (calculated from 10 cells), similar to the periodicities of AgmU and MreB.

Helical Rotor Model for Gliding Motility. To explain our observations, we propose a mechanochemical model in which PMF-driven motor proteins (MotAB homologs) run along a looped helical track (Fig. 5*A*). The axial forces exerted by the motor drive the translocation of the cell, and the tangential forces drive the rotation of the track relative to the cell membrane, cell wall, and substrate.

Our model proposes that protein "cargos" associated with the motors induce different drag forces on the substrate (Fig. 5*B*). Motors carrying large, high-drag cargos constitute the major force-generating units in the system by distorting the cell surface and generating large drag forces against the substrate via the slime (Figs. 4 and 5*B*). As the motors carry the high-drag cargos through the ventral side of the track, the helically deformed contour of the cell surface pushes on the slime (Fig. 5*B*), causing a much larger drag on the motors than elsewhere. This increased drag causes the motors to collect in "traffic jams," creating equidistant, nearly stationary clusters. These clusters resemble those observed for AglZ and AgmU, presumably constituents of

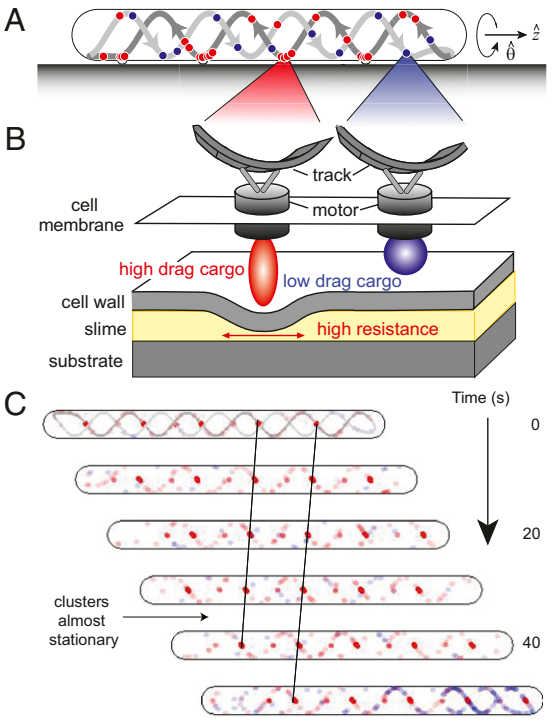

Fig. 5. Helical Rotor Model of gliding motility. (*A*) The motors push against the looped helical track (gray bands) in the same direction relative to the substrate; motors on opposite strands run in opposite directions (arrows along the bands). Blue dots are motors carrying small, low-drag cargo; red dots are motors carrying large, high-drag cargo. (*B*) Zoom-in view of the two types of motor–cargo complex. The high drag on the red cargo results from its bulky geometry, which deforms the cell envelope locally. The bump formed at the surface induces a high drag force on the motor. (*C*) Time-lapse snapshots of a computed cell viewed from the top (continuous movie, see Movie S21). The track is only shown in the first frame. The blue and red balls indicating the motors are semitransparent. When clustered, they look like one ball with brighter color. The motors carrying high-drag cargo slow down and form traffic jam clusters at the substrate interface where the external drag is highest (marked with arrows in *B*). The clusters are equally spaced by the pitch of the helical track. They move relative to the substrate much slower than the cell moves—in this computation, ≈0.4 μm/min. During the reversal, the motors carrying different cargo redistribute along the track. The cartoon compares well with the reported AglZ-GFP imaging experiments (9).

the high-drag cargo (Fig. 5*C* and Movie S21) (9, 11). In this view, the nearly stationary fluorescent patches are not "focal adhesions" in the sense of eukaryotic cell adhesions, but are aggregations of motors and cargos that provide the thrust driving gliding motility. Viewed externally, the motors driving the rotation of the helical rotor generate transverse waves on the ventral surface. These waves propagate toward the trailing pole and push on the substrate via the slime, analogous to a crawling snail (20). The low-drag cargos, although mechanically dispensable, explain the spatial localization of some other motility-related proteins, e.g., RomR, FrzCD, which may antagonize the localization of AglZ and AgmU.

Thus, in our model, the net driving force for cell movement results from the unequal distribution of high-drag vs. low-drag cargos loaded onto the motors running in opposite directions. These unequal distributions are determined by selective exchange of cargo as the motors reach the cell poles. The leading cell pole would preferentially load motors with high-drag cargos, whereas the trailing pole would load low-drag cargos. High-drag cargos are mostly traveling backward, generating net forward thrust. Cargo exchange may be controlled by an oscillator located at the cell poles that is linked to the Frz system. The oscillators are 180° out of phase because they are diffusively coupled [similar to the Min oscillator that controls cell division (21, 22)].

The model can be expressed as mechanical equations of motion (*SI Appendix*). Computer simulations of the equations reproduces the cell velocity (model 3.4 μm/min vs. experiment 2–4 μm/min) and track rotation speed of methycellulose-suspended cells (model 7.0 rpm vs. experiment 7.5 ± 1.2 rpm). The simulations show that the high-drag cargo clusters drift with a velocity ≈0.4 μm/min, too small to be distinguished experimentally.

The mechanochemical model explains the following features observed in experiments. (*i*) MotAB homologs, PMF, and MreB are all required for A-motility (the motors, powered by PMF, are predicted to move on cytoskeletal filaments); (*ii*) FRAP recovery of AgmU-mCherry is bidirectional (Movie S24) (motility proteins move in both directions because the cytoskeleton forms a closed loop); (*iii*) cells placed on soft agar, methylcellulose, or water cannot move but the AgmU helix keeps rotating (Movies S22 and S23) (There is little drag between the cargo and the super-soft external substrate and, therefore, little axial thrust. But internal drag forces between the motor, cell membrane, and cell wall remain, and they drive the rotation of the track. Detailed explanation in the *SI Appendix*.); (*iv*) cells on hard surfaces, like glass, show brighter AgmU clusters (11) (hard surfaces cause the motor proteins to slow down even more and make stronger traffic jams where the surface distortions meet the substrate); (*v*) the ≈7-min periodic reversal of cells (23, 24) (this is set by the period of the polar chemical oscillators); (*vi*) the preferential distribution of AglZ at the leading pole, as synchronized with cell reversals (9), versus RomR at the lagging pole (25) (the two proteins are assumed to be the high and low drag cargos, respectively); and (*vii*) the phenomenon of "elasticotaxis" where cells tend to orient along strain lines in the substrate (23). Details of the model and calculations are presented in *SI Appendix* and Movies S21, S22, S23, and S24.

We speculate that a similar motility mechanism may be widespread in bacteria because MreB and MotA/MotB homologs are common across a variety of bacterial species. For example, the abundant swimming cyanobacterium, *Synechococcus*, rotates about its long axis after it hits a wall, establishing a rotational component in the motility. This motion could be realized by a rotating helical track with motors running along it or motors anchored to the peptidoglycan layer driving the helical track. If the cell surface assumes a helical pattern because of the interior helix, the helix rotation would be reflected in helical waves on the surface that provide axial thrust and rotational torque (26, 27). Variations on this proposed motility mechanism could explain the behavior of other gliding bacteria such as *Cytophaga* sp. strain U67, which moves 60 times faster on glass surfaces than *M. xanthus.* An internal rotating helix could explain how latex spheres run up one side and down the other, and the observation that gliding is punctated by bouts of conical rotation about its leading pole similar to *Synechococcus* (28).

Materials and Methods

Bacterial Strains and Growth Conditions. Strains and plasmids used in this study are listed in *SI Appendix*, Table S2. *M. xanthus* strains were cultured in CYE medium, which contains 10 mM Mops at pH 7.6, 1% (wt/vol) Bacto Casitone (BD Biosciences), 0.5% Bacto yeast extract and 4 mM $MgSO_4$ (29). Five-microliter 4×10^8 cfu·ml^{-1} vegetative cultures were subjected to microscope observation directly (for the observation of cells suspended in liquid culture) or mixed with 200 μL of 1% (wt/vol) methylcellulose solution and spotted into a silicon gasket (for the observation of cells suspended in methylcellulose solution) or spotted on a thin layer of 1/2 CTT agar pad containing 1.5% (wt/vol) agar (30) (for the observation of cells gliding on agar). GST-tagged copurification and mass spectrometry were performed as described (11).

Microscopic Studies. Time-lapse and deconvolution fluorescence microscopy was performed as described (10, 11). Three-dimensional reconstructions of deconvolution images were performed with Imaris software (Bitplane). TIRF images were recorded at 2 Hz in frame-transfer mode with an electron-

multiplier gain setting of 2. FRAP images of the untreated, CCCP, and A22-treated cells were recorded at 2, 0.3, and 0.2 Hz, respectively, in frame-transfer mode with an electron-multiplier gain setting of 2. Fluorescence emission was imaged at ≈133 nm per pixel. For TIRF experiments, the distortion of cell envelope was monitored by cytoplasmic GFP expressed under the control of the *pilA* promoter (15).

ACKNOWLEDGMENTS. We thank T. Mignot, J. Shaevitz, and M. Sun for helpful discussions and sharing of recent data; J. Liphardt for providing microscope facility and valuable suggestions; L. Kohlstaedt and D. Mavrici for their help with mass spectrometry; and I.-H. Sun and L. Pan for their help with strain construction. B.N. and D.R.Z. were supported by National Institutes of Health Grant GM20509, and J.C. and G.O. were supported by National Science Foundation Grant DMS 0414039.

1. Hodgkin J, Kaiser D (1979) Genetics of gliding motility in *Myxococcus xanthus* (myxobacterales): Two gene systems control movement. *Mol Gen Genet* 171:177–191.
2. Henrichsen J (1972) Bacterial surface translocation: A survey and a classification. *Bacteriol Rev* 36:478–503.
3. Sun H, Zusman DR, Shi W (2000) Type IV pilus of *Myxococcus xanthus* is a motility apparatus controlled by the *frz* chemosensory system. *Curr Biol* 10:1143–1146.
4. Li Y, et al. (2003) Extracellular polysaccharides mediate pilus retraction during social motility of *Myxococcus xanthus*. *Proc Natl Acad Sci USA* 100:5443–5448.
5. Youderian P, Burke N, White DJ, Hartzell PL (2003) Identification of genes required for adventurous gliding motility in *Myxococcus xanthus* with the transposable element mariner. *Mol Microbiol* 49:555–570.
6. Yu R, Kaiser D (2007) Gliding motility and polarized slime secretion. *Mol Microbiol* 63: 454–467.
7. Hartzell P, Shi W, Youderian P (2008) *Gliding Motility of Myxococcus xanthus. Myxobacteria: Multicellularity and Differentiation*, ed Whitworth DE (Am Soc Microbiol, Washington, DC), pp 103–122.
8. Wolgemuth C, Hoiczyk E, Kaiser D, Oster G (2002) How myxobacteria glide. *Curr Biol* 12:369–377.
9. Mignot T, Shaevitz JW, Hartzell PL, Zusman DR (2007) Evidence that focal adhesion complexes power bacterial gliding motility. *Science* 315:853–856.
10. Mauriello EMF, Nan B, Zusman DR (2009) AglZ regulates adventurous (A-) motility in *Myxococcus xanthus* through its interaction with the cytoplasmic receptor, FrzCD. *Mol Microbiol* 72:964–977.
11. Nan B, Mauriello EMF, Sun IH, Wong A, Zusman DR (2010) A multi-protein complex from *Myxococcus xanthus* required for bacterial gliding motility. *Mol Microbiol* 76: 1539–1554.
12. Yang R, et al. (2004) AglZ is a filament-forming coiled-coil protein required for adventurous gliding motility of *Myxococcus xanthus*. *J Bacteriol* 186:6168–6178.
13. Mauriello EMF, et al. (2010) Bacterial motility complexes require the actin-like protein, MreB and the Ras homologue, MglA. *EMBO J* 29:315–326.
14. Sun H, Yang Z, Shi W (1999) Effect of cellular filamentation on adventurous and social gliding motility of *Myxococcus xanthus*. *Proc Natl Acad Sci USA* 96: 15178–15183.
15. Berleman JE, Scott J, Chumley T, Kirby JR (2008) Predataxis behavior in *Myxococcus xanthus*. *Proc Natl Acad Sci USA* 105:17127–17132.
16. Pelling AE, Li Y, Shi W, Gimzewski JK (2005) Nanoscale visualization and characterization of *Myxococcus xanthus* cells with atomic force microscopy. *Proc Natl Acad Sci USA* 102:6484–6489.
17. Lünsdorf H, Schairer HU (2001) Frozen motion of gliding bacteria outlines inherent features of the motility apparatus. *Microbiology* 147:939–947.
18. Minamino T, Imada K, Namba K (2008) Molecular motors of the bacterial flagella. *Curr Opin Struct Biol* 18:693–701.
19. Cascales E, Lloubès R, Sturgis JN (2001) The TolQ-TolR proteins energize TolA and share homologies with the flagellar motor proteins MotA-MotB. *Mol Microbiol* 42: 795–807.
20. Chan B, Balmforth NJ, Hosoi AE (2005) Building a better snail: Lubrication and adhesive locomotion. *Phys Fluids* 17:113101–113110.
21. Howard M, Kruse K (2005) Cellular organization by self-organization: Mechanisms and models for Min protein dynamics. *J Cell Biol* 168:533–536.
22. Howard M, Rutenberg AD, de Vet S (2001) Dynamic compartmentalization of bacteria: Accurate division in *E. coli*. *Phys Rev Lett* 87:278102.
23. Mauriello EM, Mignot T, Yang Z, Zusman DR (2010) Gliding motility revisited: How do the myxobacteria move without flagella? *Microbiol Mol Biol Rev* 74:229–249.
24. Zusman DR, Scott AE, Yang Z, Kirby JR (2007) Chemosensory pathways, motility and development in *Myxococcus xanthus*. *Nat Rev Microbiol* 5:862–872.
25. Leonardy S, Freymark G, Hebener S, Ellehauge E, Søgaard-Andersen L (2007) Coupling of protein localization and cell movements by a dynamically localized response regulator in *Myxococcus xanthus*. *EMBO J* 26:4433–4444.
26. Stone HA, Samuel AD (1996) Propulsion of microorganisms by surface distortions. *Phys Rev Lett* 77:4102–4104.
27. Ehlers KM, Samuel AD, Berg HC, Montgomery R (1996) Do cyanobacteria swim using traveling surface waves? *Proc Natl Acad Sci USA* 93:8340–8343.
28. Lapidus IR, Berg HC (1982) Gliding motility of *Cytophaga* sp. strain U67. *J Bacteriol* 151:384–398.
29. Campos JM, Geisselsoder J, Zusman DR (1978) Isolation of bacteriophage MX4, a generalized transducing phage for *Myxococcus xanthus*. *J Mol Biol* 119:167–178.
30. Wu SS, Kaiser D (1997) Regulation of expression of the *pilA* gene in *Myxococcus xanthus*. *J Bacteriol* 179:7748–7758.

Myxobacterial gliding motility requires cytoskeleton rotation powered by proton motive force

Beiyan Nan, Jing Chen, John C. Neu, Richard M. Berry,

George Oster* and David R. Zusman*

*To whom correspondence should be addressed. zusman@berkeley.edu, goster@berkely.edu

Supporting Materials (Experiments)

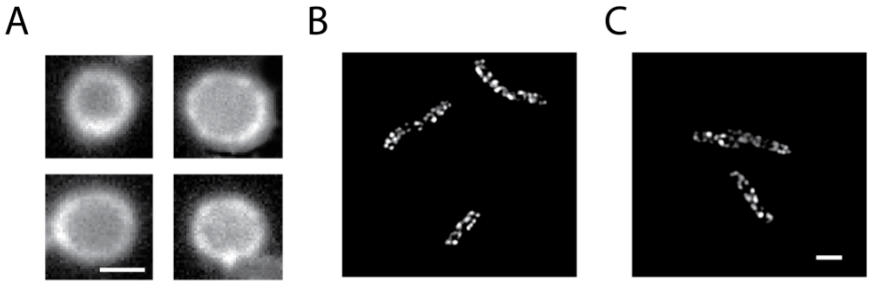

Figure S1. Elongated treatment with A22 abolishes the helical pattern of AgmU-mCherry while NaN_3 does not affect the localization and rotation of AgmU-mCherry since it has no effect on the assembly of the MreB cytoskeletal in *M. xanthus*. A) elongated treatment (>1 h) with 100 μg/ml A22 abolishes the cell shape and the helical localization pattern of AgmU-mCherry. B) and C), NaN3 has no effect on the assembly of MreB filaments. Wild type (DZ2) cells were stained with purified anti-MreB antibodies (1). B) Untreated cells. C) Cells were incubated with 80 mM NaN3 for 30 min before being fixed. Scale bar, 1 μm.

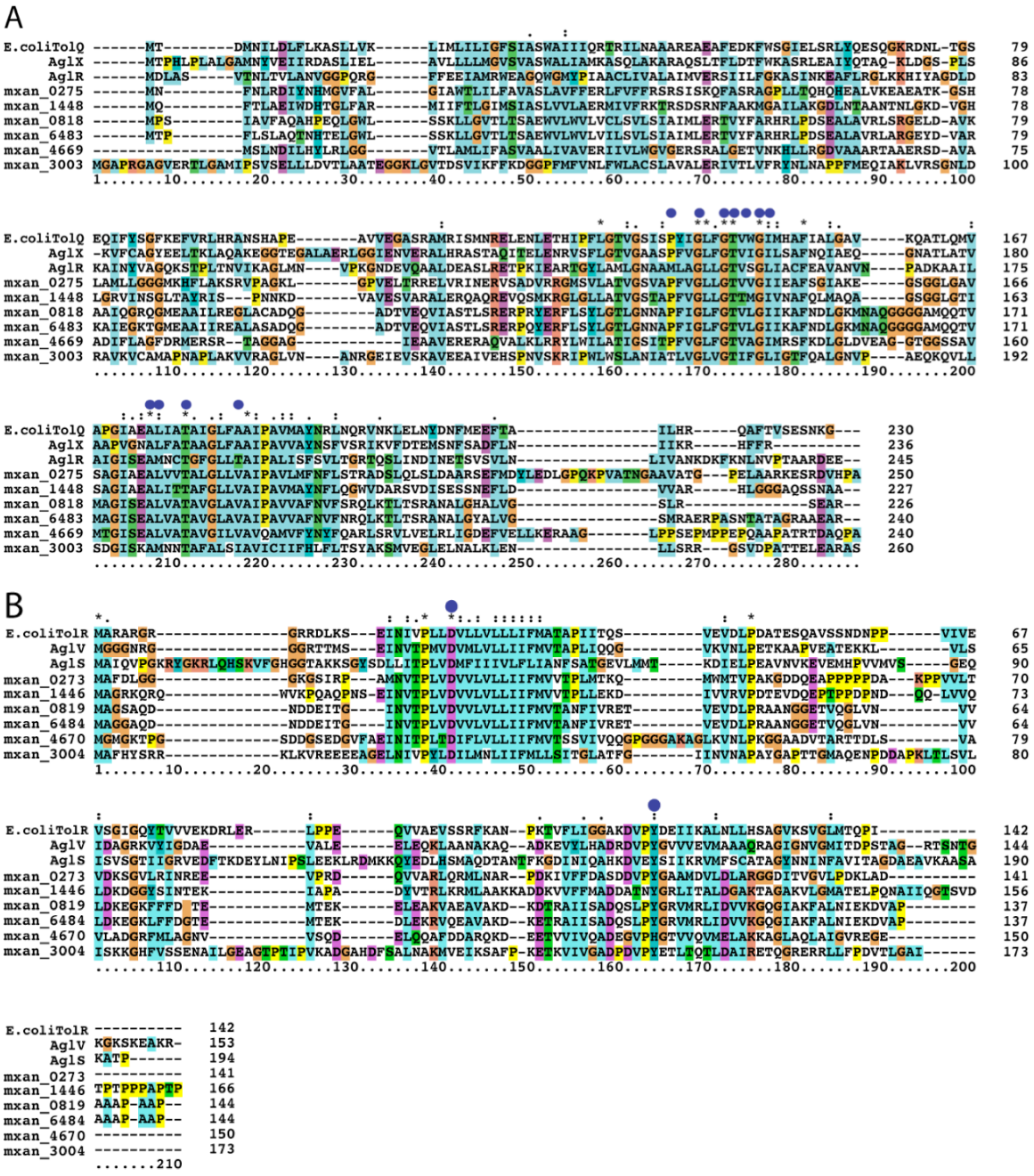

Figure S2: Sequence alignment of *E. coli* TolQ/TolR proteins and their homologues in *M. xanthus*. A) Sequence alignment of *E.coli* TolQ protein and eight *M. xanthus* TolQ homologues. B) Sequence alignment of *E.coli* TolR protein and eight *M. xanthus* TolR homologues. The residues essential for function (*2*) are marked with •.

Figure S3: The *aglX* and *aglR* strains are defective in A-motility. The movements of (*pilA*) cells that lack S-motility were monitored as an indicator of A-motility on 1.5% agar. The A-motility of the *pilA* strain is also shown. Scale bar, 50 μm.

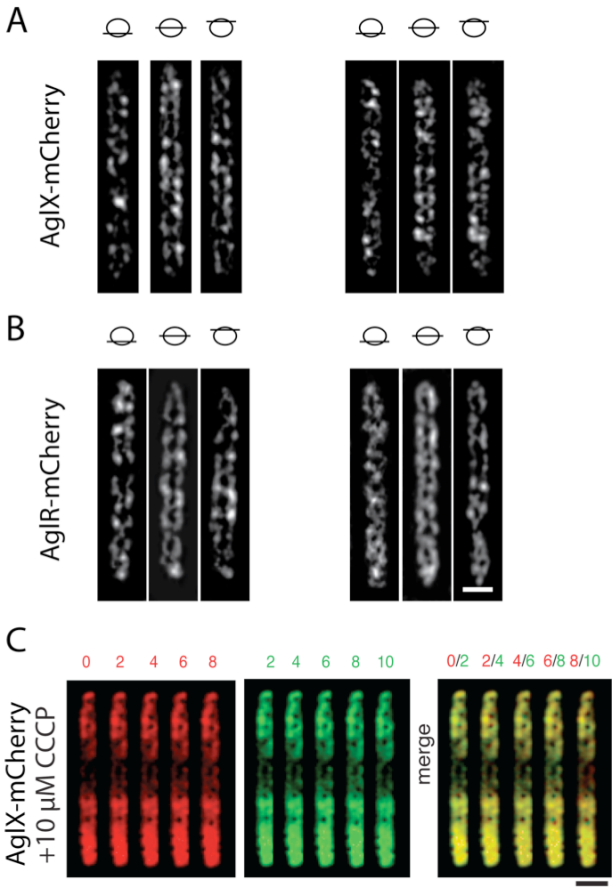

Figure S4: Localization and rotation of AglX and AglR. A) deconvolution images of AglX-mCherry. B) deconvolution images of AglR-mCherry. C) treatment of 10 μM CCCP stops the rotation of AglX-mCherry. Scale bar, 1μm.

Tables

Table S1. Previously identified A-motility proteins co-purified with GST-tagged AglX and AglV fragments.

protein	Peptide identified by mass spectrometry	Number of peptides identified
Co-purified with GST-AglX 46-167		
AglW	R.WADVGAEALVK.V	3
	R.LFNVGTGREDLKVSK.D	3
	K.VSKDAPADNASLLAHR.L	6
	R.HFTREPSPFLSR.I	1
	R.DVYVADWDGGNAR.A	5
	K.GGINILPALSQDGSQVAFTTYR.K	6
	K.NRPDIYVQSPGGEAK.A	3
	K.AVISGGQMATGAAFSPDGK.R	9
	R.IAYSLAEGESAQVYVANADGSGAR.A	2
	R.ALTDTPYGLNTSPTWSPDGKR.I	3
	R.GGSPQVYIMNADGTGVR.R	3
	R.LTFQGNYNQTPDWSPR.G	1
	R.GDLIVFTAR.D	1
	R.NAFDLFTVSVETGK.V	8
	R.LTQDQGSNEEPAFSPNGR.L	4
	R.NGGSQLYVMTADGNNQLPLRTEK.G	5
AglV	K.KLVLSIDAGR.K	49
	R.KVYIGDAEVALEELEQK.L	49
	K.EVYLHADRDVPYGVVVEVMAAAQR.A	65
	R.DVPYGVVVEVMAAAQR.A	9
	R.AGIGNVGMITDPSTAGR.T	7
AglZ	R.FAELDGEIQALQER.L	5
	K.LSQQVADLEADLAR.T	3
	R.LDKDAQEAELTQR.I	1
	R.ELSETIARNEHTEAELNANIQQQLER.I	8
	R.IGELEGEVEAVK.T	3
	R.SAKAELEADLTGQIQALTSQLEETQR.Q	6
	R.VAQLEDTVSQR.E	2
	R.ESTIESLQGDVAAR.D	2
	R.GELEATSQTLQQTHAALEDTR.G	10
	R.GALQETSDTLAHTTR.E	3
	R.IAELADLGAAK.D	7
	K.DALEQELTGQIGHLR.S	4
	R.SELSETQGNYEAER.A	7
	K.LAAESSAHIGDLTSER.D	2
	R.SELEATSQTLEQTHGQLAATR.D	1
	R.KAAASTQTTLEGQLAEAR.A	3
	R.VAELTQLTATLAQTENTR.A	2
	R.EELLQNDLTQK.G	2
	R.ITQFAQDAQTQATEADAR.A	2
	K.IQDLELAVENAQGAK.S	1
	R.LGVELQVASK.R	1
AgmU	K.IVQEYPNFER.T	2
	K.AAEFPESQVYAFALYK.Q	3
	K.TVVLYGELAGANALEKDGGK.G	1
	R.TLSNLAVTWHNEGK.K	1
	R.YADAVYSDYLTLFPENPK.A	3
	R.AAEISANLILDSYHLLQDYAK.V	2
	R.FYANDKLAVGK.F	1
	K.AQVALFNAATYR.E	2
	R.IFEHFDQLPR.R	2
	K.SRALQVVEK.K	1
	K.YVQTVTLGAPEPAICALHR.I	1
	R.ELDVYNDCAAESLK.L	2
	R.VQLIGGDLLANIQDVPPPAPK.A	2
	K.GSIVPCGGEAPCNVDVCPTR.W	2
CglB	R.WTTLQSVVPQFLENSGR.F	1
	R.TPSSDSTWTLNDDGVR.F	2
	R.ILASTPEAPVKIEVR.A	1
	R.RVEGLTGLVLSAPYLK.L	2
AgmH	K.IQVPLFVLCGAEDGVAAPAAAR.E	2
	R.VWDEQLEDPVESASALLR.A	4
AgmK	R.ALELEPDAETLGVLTALYR.R	4
	R.IQVEVAGVYER.D	1
	R.DIGDDESAVAAYR.Q	5
	R.QALELDPVNR.E	3
	R.LDHPADLLAIYER.M	3
	R.MLELSEDWR.E	5
	R.WEDLIAAYER.Q	1
	R.QLALAVSPQEQAELYVDIGNVQYQQLK.A	1
	R.SGNWPFALEMLSK.E	1
	K.EAELAGQSKDAVELYYR.L	1
	R.LGKINEDMLMDTGSAR.T	2
	K.INEDMLM*DTGSAR.T	2
	R.TAYQQALAVDPGHLPSIR.A	9
	R.EDRDTATGYWQEALK.H	6
	K.AYELDATYLPALEGYGNLLVQTR.R	3
	K.ALAIDPGHEPTLR.A	2
	R.ALVALLEK.Q	2
	R.QQLVGVLEGEAR.A	2
	R.DELHDPYMAIDAFTNALK.S	2
	K.SQPDAPEVMDQLYVLLR.E	3
	R.M*LALPALGLEPHK.A	2
	K.RVWFALGELR.R	1

protein	Peptide identified by mass spectrometry	Number of peptides identified
Co-purified with GST AglV 39-153		
AglW	K.EGMAAASINFSR.W	10
	R.WADVGAEALVK.V	16
	K.VSLAQDGGVLR.G	2
	R.LFNVGTGREDLK.V	1
	R.LFNVGTGREDLKVSK.D	2
	K.VSKDAPADNASLLAHR.L	3
	K.DAPADNASLLAHR.L	1
	R.HFTREPSPFLSR.I	1
	R.DVYVADWDGGNAR.A	11
	K.GGINILPALSQDGSQVAFTTYRK.N	6
	K.NRPDIYVQSPGGEAK.A	1
	K.AVISGGQMATGAAFSPDGK.R	3
	R.IAYSLAEGESAQVYVANADGSGAR.A	2
	R.ALTDTPYGLNTSPTWSPDGK.R	4
	R.GGSPQVYIMNADGTGVRR.L	2
	R.RLTFQGNYNQTPDWSPR.G	10
	R.LTFQGNYNQTPDWSPR.G	2
	R.NAFDLFTVSVETGKVTR.L	1
	R.LTQDQGSNEEPAFSPNGR.L	3
	R.LIVFTSTR.N	1
	R.NGGSQLYVMTADGNNQLPLRTEK.G	1
	K.GTYQTPDWSPLPQAQ.-	2
AglZ	R.IHEKDVELQGLK.M	2
	K.LQDTVLANEGEIAR.L	3
	K.LSQQVADLEADLAR.T	8
	R.IGELEGEVEAVK.T	2
	R.ESTIESLQGDVAAR.D	7
	R.GELDATSQTLQQTQQTLAQTEGALAETR.G	1
	R.IAELADLGAAKDALEQELTGQIGHLR.S	1
	K.LAAESSAHIGDLTSER.D	1
	R.KAAASTQTTLEGQLAEAR.A	1
AgmU	R.TLSNLAVTWHNEGKK.T	5
	K.LVSQLEEKKEFEK.A	1
	R.NREHYLTLWPR.A	2
	K.LYWGAPPSPDRFK.A	4
	K.YVQTVTLGAPEPAICALHR.I	4
	R.LINAPMPR.G	1
	R.AETLQEDLTDLTAQLR.S	1
AgmK	R.AFKEDPNDAAVRAR.L	1
	R.ALELEPDAETLGVLTALYR.R	1
	R.QRSWPDVASTLLR.A	2
	R.LDHPADLLAIYER.M	3
	R.WEDLIAAYER.Q	1
	R.SGNWPFALEMLSK.E	2
	K.EAELAGQSKDAVELYYR.L	1
	K.DAVELYYR.L	2
	K.INEDMLMDTGSAR.T	2
	R.TAYQQALAVDPGHLPSIR.A	4
	K.GIQEQEKDWSGYEQTLRQEAEQTEDPAAK.G	1
	R.EDRDTATGYWQEALK.H	1
	R.IARDELHDPYMAIDAFTNALK.S	2
	R.MLALPALGLEPHK.A	5

Note: 1) the chromatography experiment with each GST-tagged bait was performed twice in parallel. Each mass spectrometry indentified peptides from as many as ~100 proteins that co-purified with the bait. GST protein was used as a negative control (*3*). Only the peptides from the annotated A-motility proteins (*4, 5*) identified in both the two parallel experiments but not in the control samples are listed above. 2) AglX and AglV were co-purified with each other, suggesting that they are forming complex.

Table S2. Strains and plasmids used in this study.

strains/plasmids	genotype	reference source
M. xanthus strains		
DZ4772	*agmU::mCherry pilA::tet*	(3)
DZ4791	*agmU::mCherry mreB*^{V323A} *pilA::tet*	this study
DZ4792	*aglX::mCherry pilA::tet*	this study
DZ4793	*aglR::mCherry pilA::tet*	this study
DZ10547	*pilA::gfp/pilA+*	(*6*)
E. coli strains		
DH5α	host strain for molecular cloning	Invitrogen
BL21 (DE3) Tuner	host strain for protein expression	Novagen
plasmids		
pET28a	His-tagged protein expression vector	Novagen
pGEX-KG	GST-tagged protein expression vector	(*7*)
pBJ113	Plasmid for gene deletions/insertions, galK^{S}, kan^{R}	(*8*)
pBN10	pBJ113 with *agmU::mCherry* insertion cassette	(3)
pBN31	pBJ113 with *aglX::mCherry* insertion cassette	this study
pBN32	pBJ113 with *aglR::mCherry* insertion cassette	this study
pBN33	pGEX-KG with *gst::aglX* (AA46-167)	this study
pBN34	pGEX-KG with *gst::aglV* (AA39-153)	this study

Movies

Movie S1 and S2. Rotational motion of the AgmU-mCherry helix when *pilA*$^-$ cells are gliding on 1.5% (w/v) agar. Images were taken at 2-second intervals on the Olympus DeltaVision microscope with Rhodamine filter. The movie was obtained by processing the series of images collected with the QuickTime™ Pro software, and played with the speed of 2 frames/s.

Movie S3. Lateral view of the rotational motion of the AgmU-mCherry helix when *pilA*$^-$ cells are suspended in 1% (w/v) methylcellulose solution. Images were taken at 2-second intervals and played with the speed of 2 frames/s.

Movie S4. Polar view of the rotational motion of the AgmU-mCherry helix when *pilA*$^-$ cells are suspended in 1% (w/v) methylcellulose solution or liquid culture. The cell rotates 810° in 16 s, indicating a rotation speed of ~8.4 rpm. Images were taken at 2-second intervals and played with the speed of 2 frames/s.

Movie S5. Treated with 80 mM sodium azide on 1.5% agar, both gliding motility and AgmU-mCherry helix rotation continued for at least 30 minutes. The experiment was carried on a *pilA*$^-$ strain. Images were taken at 2-second intervals and played with the speed of 2 frames/s.

Movie S6. Treated with 80 mM sodium azide on 1.5% agar for more than one hour, most of the cells stopped gliding, but the rotation of the AgmU-mCherry helix continued. The experiment was carried on a *pilA*$^-$ strain. Images were taken at 2-second intervals and played with the speed of 2 frames/s.

Movie S7. On 1.5% agar, treatment with 10 μM CCCP stops both the gliding motility and the AgmU-mCherry rotation within 5 minutes. The experiment was carried on a *pilA*$^-$ strain. Images were taken at 2-second intervals and played with the speed of 2 frames/s.

Movie S8. On 1.5% agar, treatment with 100 μM nigericin stops both the gliding motility and the rotation of the AgmU-mCherry within 5 minutes. The experiment was carried on a *pilA*$^-$ strain. Images were taken at 2-second intervals and played with the speed of 2 frames/s.

Movie S9. On 1.5% agar, treatment with 50 μM valinomycin in the presence of 150 mM KCl does not stop the rotation of the AgmU-mCherry in one hour. The

experiment was carried on a *pilA*⁻ strain. Images were taken at 2-second intervals and played with the speed of 2 frames/s.

Movie S10. FRAP of AgmU-mCherry in *pilA*⁻ cells on 1.5% agar. Both ends of the cells were bleached, with a ~1 μm zone protected in the center. After the bleach, fluorescence recovers in a helical pattern towards both ends with the same speed and reaches both cell poles in ~10 seconds. Images were taken at 1-second intervals and played with the speed of 2 frames/s.

Movie S11. 3-D fluorescence plots of each frames of movie S10, showing the recovery of fluorescence towards both cell poles. The quantitative fluorescence plots were performed with the ImageJ software. The movie was played in the same frame rate as in movie S10.

Movie S12. FRAP of AgmU-mCherry in *pilA*⁻ cells on 1.5% agar after the treatment with 10 μM CCCP. Both ends of the cells were bleached, with a ~1 μm zone protected in the center. After the bleach, no fluorescence recovery was observed in 5 minutes. The image sequence shown in this movie contains images taken at 6-second intervals and played with the speed of 2 frames/s.

Movie S13. 3-D fluorescence plots of each frames of movie S12. No recovery of fluorescence is detectable in 5 minutes following the bleach. The quantitative fluorescence plots were performed with the ImageJ software. The movie was played in the same frame rate as in movie S12.

Movie S14. On 1.5% agar, treatment with 100 μg/ml A22, an inhibitor of MreB polymerization, stops both the gliding motility and the AgmU-mCherry rotation within 10 minutes. The experiment was carried on a *pilA*⁻ strain. The image sequence shown in this movie contains images taken at 6-second intervals and played with the speed of 2 frames/s.

Movie S15. FRAP of AgmU-mCherry in *pilA*⁻ cells on 1.5% agar after the treatment with 100 μg/ml A22. Both ends of the cells were bleached, with a ~1 μm zone protected in the center. After the bleach, no fluorescence recovery was observed in 5 minutes. The image sequence shown in this movie contains images taken at 6-second intervals and played with the speed of 2 frames/s.

Movie S16. On 1.5% agar, treatment with 200 μg/ml A22 on an *mreB* ^{V323A} *pilA*$^{-}$ strain does not stop the rotation of AgmU-mCherry. Images were taken at 2-second intervals and played with the speed of 2 frames/s.

Movie S17. On 1.5% agar, treatment with 100 μM cephalexin for 8 h makes cells elongated but does not stop the rotation of AgmU-mCherry. Images were taken at 2-second intervals and played with the speed of 2 frames/s.

Movie S18. On 1.5% agar, treatment with 100 μM vancomycin for 2 h does not stop the rotation of AgmU-mCherry. Images were taken at 2-second intervals and played with the speed of 2 frames/s.

Movie S19. Rotational motion of the AglX-mCherry helix when *pilA*$^{-}$ cells are gliding on 1.5% agar. Images were taken at 2-second intervals and played with the speed of 2 frames/s.

Movie S20. Rotational motion of the AglS-mCherry helix when *pilA*$^{-}$ cells are gliding on 1.5% agar. Images were taken at 2-second intervals and played with the speed of 2 frames/s.

Supporting Materials (Theory)

We have constructed a model that explains the mechanics of A-motility in myxobacteria. The basic elements consist of proton driven motors running along a rigid single continuous-loop track folded into a double helix (Figure 4A in the main text, grey lines). The forces in the axial direction drive the translocation of the cell, and the forces in the angular direction drive the rotation of the track. We assume that all the motors run in the same direction along the track. This is for convenience of calculation; relaxing this assumption does not change the force-generating mechanism, but requires different parameters to reproduce the experiment data. Due to the looped topology of the track the motors run in opposite directions relative to the substrate when they are on the opposite strands of the helical track.

The motors are loaded with two kinds of 'cargo', causing different drag against the substrate (Figure 5A in the main text, red indicates high-drag, blue indicates low-drag). The cargo consists of A-motility related proteins (AMRP), such as AglZ and AgmU. In Figure 5A in the main text, we suggest that a geometric factor underlies the differences in the drag force. The large size of the high-drag (red) cargo creates a bump on the surface of the cell envelope. As a motor drives a high-drag cargo along the helix, the bump encounters a large drag force between the cell and the substrate due to the viscous slime, and the motor slows down significantly at the ventral surface. The 'traffic jams' of slow-moving motors at the substrate interface appear in the experiments as periodic fluorescent spots, or bars, that reflect the helical periodicity of the helical rotor. Because most of the high-drag motors accumulate in the traffic jams at the substrate interface, it is at these loci that the bulk of the propulsive force is generated.

A net driving force is generated when the two strands of the track bear different numbers of motors carrying high-drag vs. low-drag cargo. This can be realized by exchanging the cargo at different rates as the motors pass through the polar region. At the leading pole the motors tend to shed the low-drag cargo and take on a high-drag one, and vice versa at the trailing pole. The mechanism for this exchange is discussed later. Then more high-drag motors will travel from the leading pole to the trailing pole than in the opposite direction. Thus the net force on the cell drives it towards its leading pole. In other words, the relative cargo exchange rates at the poles determine the direction of cell motion. When the rates switches, the cell reverses.

Recent experiments show that cell reversal is controlled by diffusion-coupled biochemical oscillators at the opposite poles (9). Without sufficient information about the biochemical pathway, we borrowed from the existing models for the Min oscillator and used it as the master oscillator in our model (10-12). We rescaled the parameters to achieve an oscillation period around 7 min ×2 (7 min is time between reversals, i.e. the half period) in a 5 μm long cell. We emphasize that any pair of diffusion-coupled limit cycle oscillators (e.g. the Fitzhugh-Nagumo system (e.g. 13)) will give similar results. The master oscillator controls the periodic dynamics of the cargo exchange rates at the poles.

The basic features of the mechanical model are:

1. Motors run in a uniform direction along the helical track, i.e. in opposite directions relative to the substrate when on opposite strands of the closed helical track.
2. Motors carry either large, high-drag or small, low-drag cargo. The high-drag cargo encounters very high viscous resistance at the substrate interface, and slows down to form 'traffic jams'. These motor aggregations constitute the major force generating units driving cell locomotion.
3. Motors exchange cargo at the poles, with different exchange rates so as to achieve unequal distributions of the high-drag and low-drag motors on the two strands.
4. Cells reverse when the relative cargo exchange rates switch at the poles; these switches are controlled by diffusion-coupled anti-phased biochemical oscillators at the cell poles.

Figure S5 shows the force balance on each motor. The forces indicated in all the three panels must sum to zero. The subscript *M* stands for motor, *C* for cell membrane/cell wall, *S* for substrate, and *H* for helix. For simplicity we assume that the cell membrane and cell wall are held together with no relative motion. They are regarded as one mechanical part in the model. The motor exerts a force $F_{//}$ along the helix. There is also a transverse force, $F_{\perp}$, perpendicular to the arc length that keeps the motor on the track. The force exerted by the membrane/wall on the ith motor is assumed to be purely a drag force, $\mathbf{F}^i_{MC} = -\zeta^i_{MC}\mathbf{V}^i_{MC}$, where $\mathbf{V}^i_{MC} = \mathbf{V}^i_{MH} + \mathbf{V}_{HC}$ is the relative velocity between the motor and the membrane/wall. Here ζ^i_{MC} is the drag coefficient that accounts for the drag on the motor both from the cell membrane and from the cell wall. As the motor carries the high-drag cargo through the substrate interface, it encounters another drag caused by the resistance between the bump and the substrate. This force is proportional to the relative velocity between the motor and the substrate, i.e. $\mathbf{F}^i_{MS} = -\zeta^i_{MS}\mathbf{V}^i_{MS}$ with $\mathbf{V}^i_{MS} = \mathbf{V}^i_{MH} + \mathbf{V}_{HC} + \mathbf{V}_{CS}$. We assume that the drag coefficient ζ^i_{MS} applies only to the high-drag motor at the substrate interface and is 0 otherwise. Because we assume that only the track rotates, it holds that $\mathbf{V}_{HC} = r\omega_H\hat{\theta}$ and $\mathbf{V}_{CS} = V_C\hat{z}$, where *r* is the radius of the cross section of the cell, V_C is the cell velocity, *and* ω_H is the angular velocity of the helix rotation. $\hat{z}$ and $\hat{\theta}$ are unit vectors in the axial and rotational direction respectively. The force balance equation on a motor is written as Eq.(S1).

In addition, there are two force balance equations (FBE) describing to the rotation of the track (Eq. (S2)) and the translocation of the cell (Eq. (S3)). ζ_{Hrot} is the rotational drag coefficient of the track, ζ_C is the translational drag coefficient of the cell.

FBE on the motor: $$\mathbf{F}^i_{MH} + \mathbf{F}^i_{MC} + \mathbf{F}^i_{MS} = 0 \quad \text{(S1)}$$

FBE for track rotation: $$\zeta_{Hrot}\omega_H = -\sum_i \mathbf{F}^i_{MH}\cdot\hat{\theta} \quad \text{(S2)}$$

FBE for cell translocation: $$\zeta_C V_C = \sum_i \mathbf{F}^i_{MS}\cdot\hat{z} \quad \text{(S3)}$$

The cell translocation is driven only by the external reaction force to the drag forces between the motors and the substrate, $\mathbf{F}^i_{MS}$. But the track rotation is driven by $-\mathbf{F}^i_{MH} = \mathbf{F}^i_{MS} + \mathbf{F}^i_{MC}$, i.e. both the external forces and the internal forces between the motors and the cell membrane/cell wall. This difference is necessary to explain why the track rotates in cells that are not moving: this happens when the external traction vanishes ($\mathbf{F}^i_{MS} = 0$) but the internal forces remain ($\mathbf{F}^i_{MC} \neq 0$), as in cells suspended in methylcellulose.

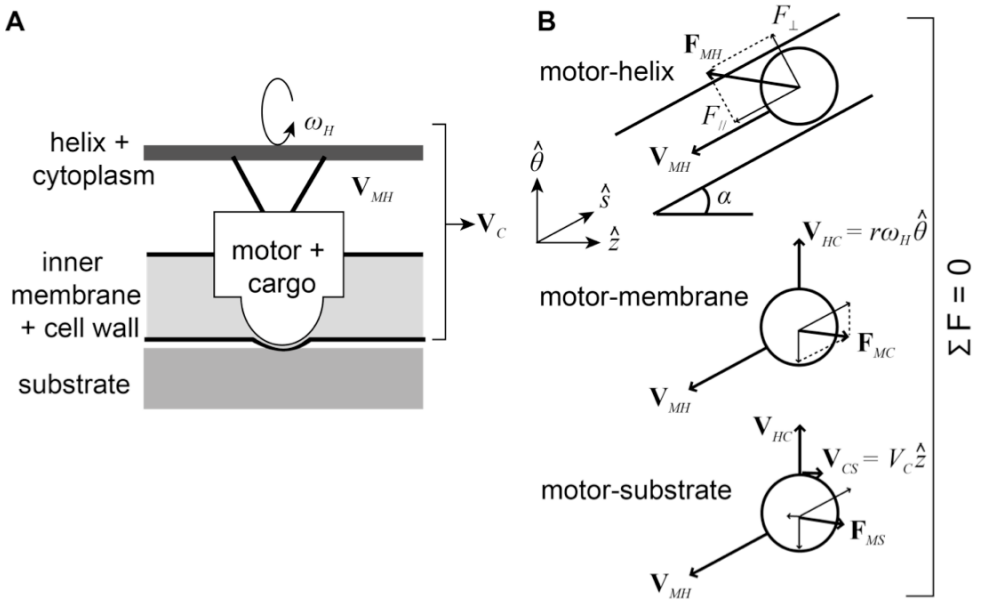

Figure S5: Force balance on a single motor. (**A**) Side view showing the mechanical components of the system. The cell membrane and cell wall are considered as one part, with no relative motion between each other. (**B**) Top view showing the force balance. *F*: forces, *V*: velocities. The velocities are projected onto the substrate surface. The force between the motor (*circle*) and the helix (*area between two parallel lines*) along the helical direction, $F_{//}$, results in the motor velocity $\mathbf{V}_{MH}$. There is also a transverse force, $F_{\perp}$, perpendicular to the helical arc length that keeps the motor on the track. The cell membrane is assumed to stick with the cell wall. They combine into one mechanical component. The force between the motor and the membrane/wall, $\mathbf{F}_{MC}$, and the one between the motor and the substrate, $\mathbf{F}_{MS}$, are assumed to be purely drag forces. They act opposite to the relative velocities between the involved parts, and proportional up to a drag coefficient. The thicker arrows show the vectorial sums of the composite forces. Here we assume that the helical track is the only rotational component, whereas the cell membrane/cell wall does not rotate (constrained by much larger rotational drag coefficient). Then it holds that $\mathbf{V}_{HC} = r\omega_H\hat{\theta}$ and $\mathbf{V}_{CS} = V_C\hat{z}$, where V_C is the cell velocity and ω_H is the angular velocity of the helix rotation. $\hat{z}$ is the unit vector in the axial, $\hat{\theta}$ is the unit vector in the rotational direction, and $\hat{s}$ is the unit vector tangent to the direction of the helix.

The model was simulated in Matlab™ using an agent-based algorithm. The motion and cargo attachment of 1000 motors were traced in the simulation. The cell velocity, track

rotation speed, as well as the motor velocities along the track were determined from Eq. (S1)-(S3) for each time step. The motor velocities were calculated taking into account Brownian motion. When a motor reaches the pole, the cargo exchange was executed with a probability set by the biochemical oscillators.

With the parameters listed in Table S3, the computed cell velocity is ~3.4 μm/min (blue solid line in Figure S6A), falling in the experimental range of 2−4 μm/min. The cell rotates at a speed ~3.8 rpm (green dashed line in Figure S6A). Controlled by the master oscillators, the cell translocation and the track rotation reverses periodically about every 7 min.

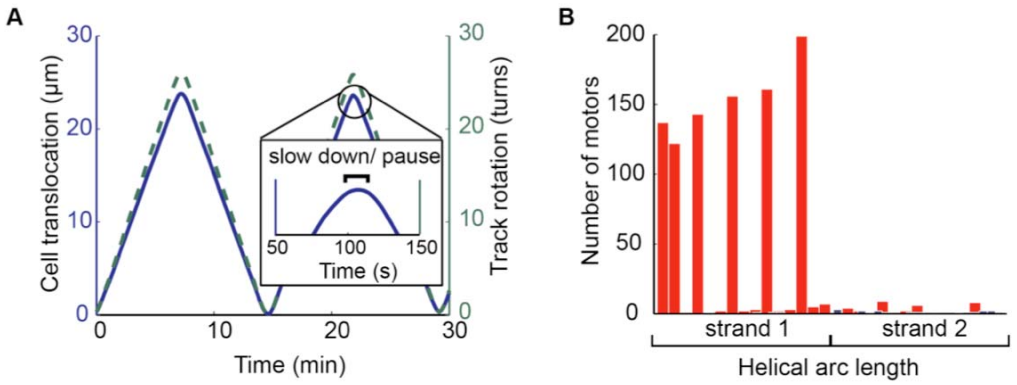

Figure S6: The results of the calculations. Parameters used in the calculation are listed in Table S3. (**A**) The time trajectories of the cell translocation (*blue solid line, left axis*) and the track rotation (*green dashed line, right axis*). The translocation and rotation show periodic reversal with synchronized phases. The cell moves at ~3.4 μm/min and the track rotates at ~3.7 rpm. The inset is a zoomed-in view around the reversal showing a short interval of nearly zero velocity. (**B**) A sample of the distribution of motors along the track. Red columns: number of high-drag motors; blue columns: number of low-drag motors. The high-drag motors form equidistant clusters (*tall red columns*). Most high-drag motors run from the leading pole to the trailing pole, because the leading pole tends to equip the motors with high-drag cargo. So the clusters only appear on the helical strand that supports the leading-to-trailing motion at the moment. Due to the significantly reduced velocity in the clustered regions, most motors are trapped there, with only a small number of motors distributed elsewhere.

The dynamics of the AMRP clusters along the cell-substrate interface are explained by the model. The motors carrying high-drag cargo cluster in traffic jams at the substrate interface (Figure S6B, Figure 5B-C in the main text, movie S21) because they are slowed down there. The clusters are localized along the helical strand that currently supports the leading-to-trailing directed motors; they appear equally spaced by the pitch of the helical track. Occasionally a motor picks up a high-drag cargo from the trailing pole, and is slowed down at the substrate interface as it runs towards the leading pole. Because the probability is small, such a motor can find few companions to form cluster before it reaches the other pole. Relative to the surface, the high-drag clusters drift towards the trailing pole relative to the substrate, but with a velocity ~0.4 μm/min, much smaller than

the cell velocity. Such a small drift is hardly distinguishable in current experiments. The FRAP experiments are also explained by the model. The fraction of motors originated from a certain region of the track spreads out to the whole track in a few seconds (Movie S24).

Upon reversal the cell slows down to near stall (inset of Figure S6A), corresponding to the 10-sec pause observed in the experiments. This occurs because the motors must redistribute along the helix, causing a transition period during which the numbers of high-drag motors become more balanced in the two directions so that the driving forces largely cancel out. If we take into account the viscoelastic property of the slime surrounding the cell, the cell should virtually stop when the driving force per unit area drops below the yield stress of the slime. This may account for the short pauses shown in the experiments (14).

The behaviors of cells suspended in methylcellulose are also explained by the model. The closed helical track, however, rotates at 7−8 rpm (**Figure S**8A, movie S22 and S23). Also, the AMRPs do not form clusters anywhere along the cell body. Methylcellulose forms ‘super-soft’ viscoelastic ‘substrate’ around the cell. In the model, if we reduce ζ_{MS} to 0, the computed rotational speed is ~7.0 rpm, compatible with the measured 7.5±1.2 rpm. The track also reverses its direction of rotation every 7 min.

The rotation persists because the high-drag motor has a larger drag coefficient against the cell wall than does the low-drag motor. The difference in the internal force balance drives the rotation of the track, but does not contribute to cell translocation. In reality, there may be a small drag between the high-drag cargo and the methylcellulose, creating a small driving force for cell translocation, but the cell will remain immobile if the driving force is smaller than the yield stress of the methylcellulose.

Table S3: Parameters used in the mechanical model.

Parameters	Meaning	Values	Source
N	number of motors	1000	< ~20 μm total length of track ÷ 10 nm diameter of BFM stator
F_M	motor force along the helical direction	1 pN	150 pN·nm torque of BFM stator[1] ÷ 20 nm radius of BFM rotor[2] ≈ 7 pN
ζ_{MB}^{L}	drag coeff. between motor and membrane/wall for low-drag motor	0.1 pN·s/μm	k_BT ÷ 0.04 μm^2/s diffusion coeff. of proteins on plasma membrane[3]
ζ_{MB}^{H}	drag coeff. between motor and membrane/wall for high-drag motor	0.5 pN·s/μm	> ζ_{MB}^{L}
ζ_{MS}	drag coeff. between the high-drag cargo and the substrate for high-drag motor	150 pN·s/μm	bounded by small drift velocity
φ	range of angle considered as substrate interface [-φ/2, φ/2]	π/15	width of AglZ clusters in the fluorescence images[4]
ζ_C	translocation drag coeff. of the cell	2×10^4 pN·s/μm	10 pili working simultaneously × 100 pN pilus force[5] ÷ 3 μm/min cell velocity
ζ_{Hrot}	rotational drag coeff. of the track	500 pN·s	fit rotation speed
p	pitch of helix	1 μm	pitch of MreB / AgmU-mCherry[6]
r	radius of helix	0.2 μm	AglZ 3D localization[7]

[1] See Reid, Leake et al. 2006; Sowa and Berry 2008.
[2] See Sowa and Berry 2008.
[3] See Adams, Chen et al. 1998; Lippincott-Schwartz, Snapp et al. 2001.
[4] See Mignot, Shaevitz et al. 2007.
[5] See Maier, Potter et al. 2002.
[6] See main text.
[7] Estimated from Mauriello et al. 2009.

Because the external drag coefficient is nearly zero everywhere, the high-drag motors can not form clusters (Figure S7 and Figure S8B). The high-drag motors and low-drag motors mainly distribute on opposite strands. Such a distribution is caused by the unequal cargo exchange rate at the poles, as in the substrate-supported case above. Between the reversals, there are usually more high-drag motors than low-drag ones. This is because the high-drag motors travel slower, thus by flux balance of motors they achieve higher density.

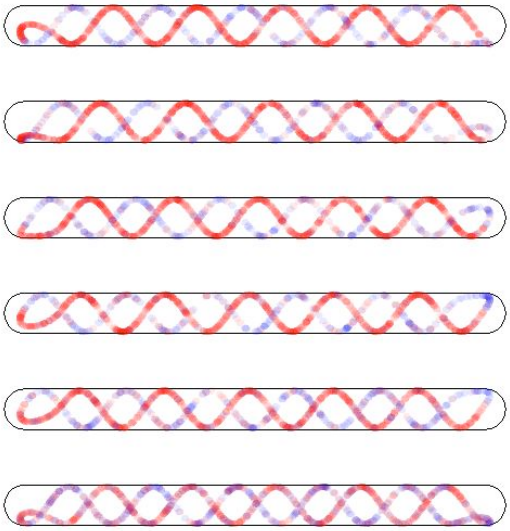

Figure S7: Time-lapse snapshots for cells suspended in methylcellulose viewed from the top. See Movies S22 for top view and Movie S23 for head-on view (compare to experimental movie S8). Black line: cell envelope; blue balls: motors carrying low-drag cargo; red balls: motors carrying high-drag cargo. The high-drag and low drag motors are distributed along opposite strands. The motors do not form clusters as those shown in Figure 5B-C in the main text.

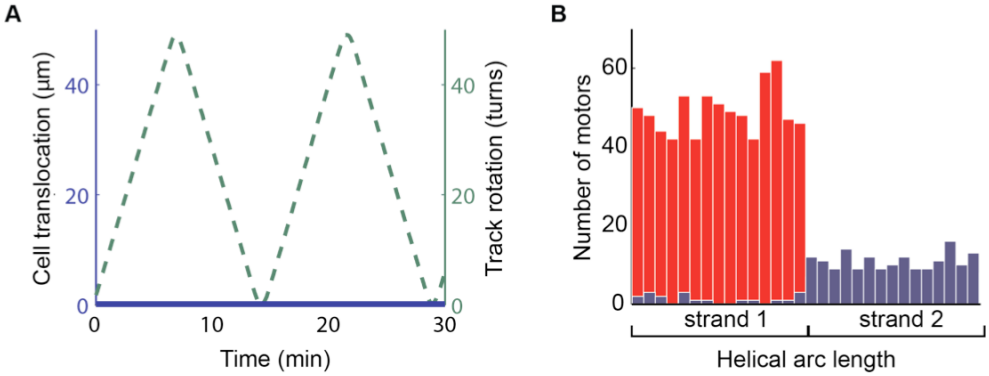

Figure S8: Results for cells suspended in methylcellulose. Parameters used in the calculation are listed in Table S3, except for $\phi = 2\pi$, and $\zeta_{MS} = 0$. All the legends follow those in Figure S6. (**A**) The translocation of the cell (*blue solid line, left axis*) and the rotation of the helical track (*green dashed line, right axis*). The track rotates at ~7.0 rpm. The rotation maintains the periodic reversal for every 7 min or so. The cell does not translocate because with $\zeta_{MS} = 0$ there is no external

forces against the methylcellulose gel. (**B**) The distribution of motors along the track at a sample moment. The high-drag (*red*) motors are mostly located on one strand and the low-drag (*blue*) motors mostly located on the other, running in the opposite direction. The high-drag motors do not form clusters along the cell body. There are more high-drag motors because they move slower along the track.

Finally, the model also explains several other observations, which will be dealt with elsewhere. These include (i) the tendency of cells to orient along stress wrinkles in the substrate (so called 'elasticotaxis' (15); (ii) the dynamics of AMRP concentrations at the poles; (iii) the motions of beads attached to the cell. These will be addressed in a separate publication, and (iv) the swimming of *Synechococcus* can be explained quantitatively by a modification of the helical-rotor model.

Movies

Movie S21: Cartoon movie illustrating the computed result for a cell gliding on a surface (top view, sped up by 60 times). The cell reverses periodically. The high-drag motors cluster at the cell-substrate interface. The distribution becomes more dispersed about the cell reversal.

Movie S22: Cartoon movie illustrating the computed result for a cell suspended methylcellulose (top view, sped up by 60 times). The track rotates ~ 7 rpm and reverses the direction periodically. The cell does not translocate and the motors do not cluster. The high-drag (red) and low-drag (blue) motors are largely distributed on opposite strands of the track.

Movie S23: Cartoon movie illustrating the computed result for a cell suspended methylcellulose (polar view, sped up by 60 times). The track rotates ~ 7 rpm and reverses the direction periodically. This movie compares well with experimental movie S4.

Movie S24: Cartoon movie illustrating the computed result for the FRAP experiment in moving cells (top view, sped up by 60 times). The motors start in a narrow region along the helical track and disperse throughout the track in a short while (compare to experimental movie S10).

References

1. Mauriello EMF*, et al.* (2010) Bacterial motility complexes require the actin-like protein, MreB and the Ras homologue, MglA. *EMBO J* 29:315-326.
2. Goemaere EL, Cascales E, & Lloubes R (2007) Mutational analyses define helix organization and key residues of a bacterial membrane energy-transducing complex. *J Mol Biol* 366:1424-1436.
3. Nan B, Mauriello EMF, Sun I, Wong A, & Zusman DR (2010) A multi-protein complex from *Myxococcus xanthus* required for bacterial gliding motility. *Mol. Microbiol.* 76:1539-1554.
4. Youderian P, Burke N, White DJ, & Hartzell PL (2003) Identification of genes required for adventurous gliding motility in *Myxococcus xanthus* with the transposable element mariner. *Mol Microbiol* 49:555-570.
5. Hartzell P, Shi W, & Youderian P (2008) Gliding Motility of *myxococcus xanthus*. *Myxobacteria: Multicellularity and Differentiation.*, ed Whitworth DE (ASM Press), pp 103-122.
6. Berleman JE, Scott J, Chumley T, & Kirby JR (2008) Predataxis behavior in *Myxococcus xanthus*. *Proc Natl Acad Sci U S A* 105:17127-17132.
7. Guan KL & Dixon JE (1991) Eukaryotic proteins expressed in *Escherichia coli*: an improved thrombin cleavage and purification procedure of fusion proteins with glutathione S-transferase. *Anal Biochem* 192:262-267.
8. Julien B, Kaiser AD, & Garza A (2000) Spatial control of cell differentiation in *Myxococcus xanthus*. *Proc Natl Acad Sci U S A* 97:9098-9103.
9. Zhang Y, Franco M, Ducret A, & Mignot T (2010) A bacterial Ras-like small GTP-binding protein and its cognate GAP establish a dynamic spatial polarity axis to control directed motility. *PLoS Biol* 8:e1000430.
10. Howard M, Rutenberg AD, & de Vet S (2001) Dynamic Compartmentalization of Bacteria: Accurate Division in *E. coli*. *Physical Review Letters* 87:278102.
11. Howard M & Kruse K (2005) Cellular organization by self-organization: mechanisms and models for Min protein dynamics. *J. Cell Biol.* 168:533-536.
12. Fischer-Friedrich E, Meacci G, Lutkenhaus J, Chaté H, & Kruse K (2010) Intra- and intercellular fluctuations in Min-protein dynamics decrease with cell length. *Proc Natl Acad Sci U S A* 107:6134-6139.
13. Murray JD (2002) *Mathematical biology* (Springer, New York) 3rd Ed pp xxiii, 551.
14. Mignot T, Shaevitz JW, Hartzell PL, & Zusman DR (2007) Evidence that focal adhesion complexes power bacterial gliding motility. *Science* 315:853-856.
15. Fontes M & Kaiser D (1999) *Myxococcus* cells respond to elastic forces in their substrate. *Proc Natl Acad Sci U S A* 96:8052-8057.